Design, Development, and Control for the Self-Stabilizing Bipedal Exoskeleton Prototype Co-Ex

Ahmed Fahmy Soliman, *Student Member, IEEE,* Sinan Coruk, Mehmet C. Yildirim, *Student Member, IEEE,* Deniz Ugur, Suleyman Can Cevik, Burak Ozkaynak, Polat Sendur, and Barkan Ugurlu, *Senior Member, IEEE*

***Abstract*—This article presents the design, development, and implementation of walking control for the bipedal exoskeleton prototype Co-Ex. The main objective in developing this prototype is to take a successive step towards ambulatory support via an exoskeleton with self-stabilization capability. To attain this goal, Co-Ex is equipped with 8 torque-controllable active joints to provide ambulatory support while ensuring improved environmental interaction. The development of Co-Ex led to three contributions: i) self-stabilization capability in 3D against external disturbances, ii) a locomotion control framework that provides dynamically balanced walking behaviour in 3D despite the underactuated leg configuration, and iii) a power-aware leg design in which most actuators are deployed around the waist for reduced leg inertia. To verify the self-stabilization and locomotion capabilities of Co-Ex, we conducted a series of experiments using a dummy manikin. As a result, Co-Ex showed self-stabilisation behaviour against disturbances and exhibited favourable locomotion characteristics that validated the proposed approach.**

***Index Terms*—lower body exoskeleton, balance control, locomotion control, torque control.**

I. Introduction

RECENT developments in exoskeleton technology led to successful applications in providing ambulatory support and power assistance to both able-bodied users and SCI (Spinal Cord Injury) patients. In particular, quadrennially organized Cybathlon events showcased the effectiveness of lower-body exoskeletons as several SCI patients competed with each other in completing the daily activities [1]. Although there are reports that question the functionality of such systems [2], clinical studies indicated the potential benefits of these devices [3], and their effectiveness may be enhanced with further research by addressing persistent challenges [4].

One particular issue regarding most current-day exoskeletons is providing ambulatory support while effectively counteracting external perturbations. Accordingly, this paper aims to contribute to this challenge with the proposal of a self-stabilizing exoskeleton prototype that includes the least possible number of active joints to contain weight and energy consumption. In the following subsections, a succinct literature review is introduced, along with our contributions. In Sections II and III, the mechatronic hardware of the proposed exoskeleton prototype and its controller scheme are explained. In Section IV, experimental results are presented, and finally, the paper is concluded in Section V.

Manuscript received XXXXXX XX, 20XX; revised XXXXXX XX, 20XX. *(Corresponding author: Barkan Ugurlu.)*

A. F. Soliman, S. C. Cevik, B. Ozkaynak, P. Sendur and B. Ugurlu are with the Dept. of Mechanical Engineering, Ozyegin University, 34794 Istanbul, Türkiye. e-mail: (barkan.ugurlu@ozyegin.edu.tr).

S. Coruk is with Repkon Machine and Tool Industry and Trade Inc., 34980 Istanbul, Türkiye.

M. C. Yildirim is with the Chair of Robotics and Systems Intelligence (RSI) and the Munich Institute of Robotics and Machine Intelligence (MIRMI), Technical University of Munich (TUM), 80333 Munich, Germany.

D. Ugur is with the School of Computing Science, Simon Fraser University, Burnaby, BC V5A 1S6, Canada.

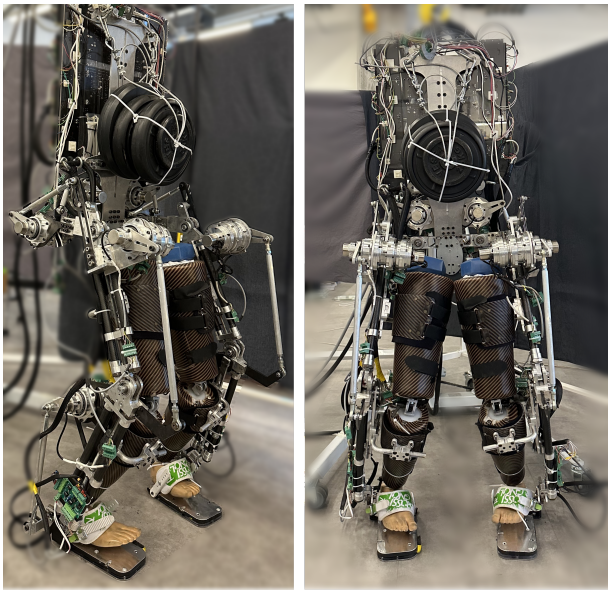


Fig. 1: The bipedal exoskeleton prototype Co-Ex, while supporting a dummy manikin with passive joints.

A. State-of-the-art

When examining the state-of-the-art, one can observe that a great majority of lower body exoskeletons actively assist users through their hip and knee F/E (Flexion/Extesion) joints to improve energy economy, cost, and weight [5]–[8]. Therefore, users must actively engage their upper limbs via crutches to maintain balance when using these 2 active DoFs (Degrees of Freedom) per leg exoskeletons. It is possible to reduce upper body effort through the use of active compliance for such systems [8]. However, overdependence on crutches as the sole means of support may lead to severe pain and shoulder joint problems [9]. Hence, exoskeletons with self-stabilization capability appear to be an essential requirement in robot-aided walking [10], [11].

To ensure dynamic balance along the sagittal plane, the human ankle joint must be actively supported through the

D/PF (Dorsi/Plantar Flexion) axis [12]. To this end, researchers developed various lower-body exoskeletons that have 3 active joints along the hip, knee, and ankle joints [13]–[15]. In particular, experimental results reported in [14] and [15] demonstrated the active balancing capability under certain levels of disturbances, underlining the importance of active ankle joint support through the D/PF axis.

While providing support through the sagittal plane is a leap forward in exoskeleton technology, balancing in 3D space dictates the presence of active joints that enable the CoM (Center of Mass) to sway along the coronal plane. The studies in both healthy and impaired human biomechanics have pointed out the importance of hip abductors for stable gait generation [16], [17]. In a simulation study, it was observed that human gait is quite sensitive to hip abductors [18], and any fatigue related to this joint can affect the whole leg kinematics [19]. In light of this information, it is argued that exoskeletons with active hip A / A joints (Adduction / Abduction) could provide relatively more comprehensive walking support [20]. As such, these exoskeletons are equipped with 4 active joints per leg along hip A/A and F/E, knee F/E, and ankle D/PF axes.

Further increase of active joints allows hands-free walking support in 3D via quasi-static and dynamic gaits [11], [21]. The REX exoskeleton can provide 3D walking support, yet could generate only slow and quasi-static gaits [21]. The Atalante exoskeleton, on the other hand, could provide 3D walking support without technical assistance. Similar to conventional humanoids, Atalante has 6 active joints per leg. In [11], Kerdraon et al. demonstrated that Atalante was effective in providing ambulatory support to patients with SCI, making it one of the most advanced devices of its kind.

B. Contributions

1) Self-Stabilization in 3D Despite Underactuation: On one side of the spectrum, there are conventional exoskeletons that heavily tax users' upper body to maintain quasi-static balance. On the other side, exoskeletons with fully-actuated legs, e.g., Atalante [11], can address hands-free walking aid; yet there could be an optimal compromise between these two specimens. Considering the robust stabilizers [22]–[25], we argue that self-stabilization could be attained with exoskeletons that possess 4 active joints per leg, covering the fundamental aspects of walking, i.e., complete support through hip A/A and F/E, knee F/E, and ankle D/PF [15], [16], [18], [20], [26]. Compared to fully actuated systems, decreasing the total number of active joints from 12 to 8 enables us to improve power requirement and energy autonomy while reducing the hardware complexity and total mass. Although hands-free walking may not be possible with such an exoskeleton due to its low structural stiffness [27], we experimentally demonstrated self-stabilization capability in 3D against external disturbances. Whilst there are attempts for self-balancing exoskeletons [15], [28], Co-Ex is the first underactuated exoskeleton with self-stabilization capability in 3D through sagittal and coronal planes, despite the dummy manikin with unknown mass and mass distribution.

2) Locomotion Control for Underactuated Exoskeletons: The underactuated leg configuration prevents the independent control of foot position and orientation; thus, the exoskeleton foot may land obliquely during touch-down, severely impairing the balance. To overcome this issue, we synthesized a locomotion controller that sorts the trajectory tasks hierarchically concerning their priority levels. The controller formulates this issue using an optimization problem in which the tasks with lower priority are achieved without tempering with the tasks with higher priority. Combining this controller with a posture controller and full-body dynamics, we constructed a locomotion control framework, enabling our underactuated bipedal exoskeleton to exhibit dynamic walking with no oblique foot landing. This feature potentially paves the way for reduced upper body engagement compared to conventional quasi-static walking. We argue that the proposed locomotion controller is applicable to other underactuated exoskeletons with a similar joint configuration [20], [28].

3) Power-Aware Exoskeleton Leg Design: Another challenge arises in bedding the motors since exoskeletons must be wearable. The straightforward approach suggests the collocation of joint and motor axes, e.g., [13], which may lead to increased inertia of the leg mechanisms relative to the hip joint. As a result, torque and power demands may also increase. On the contrary, the inverted pendulum model could provide energetically less costly trajectories in which the support leg imitates a pendulum [26]. To this end, this paper proposes a leg structure in which most motors are bedded around the waist such that the robot mass is condensed around the hip joint for reduced leg inertia while containing the power requirement.

II. Mechatronics Hardware Design

A. General Structure

The idea of providing a **Co**mpliant **Ex**oskeleton for dependable human-robot **Co-Ex**istence led to the development of *Co-Ex*. It is a fully torque-controllable bipedal exoskeleton prototype capable of maintaining its balance in 3D, aiming to provide dependable ambulatory support. In Fig. 1, the actual robot is displayed with a dummy manikin.

Fig. 2 depicts the joint configuration of Co-Ex. Each leg has 4 active joints: a 2 DoF hip joint that can rotate along the A/A and F/E axes, a knee joint that allows motions along the F/E axis, and finally, an ankle joint that can rotate along the D/PF axis. When designing the mechanical parts, straightforward mechanical engineering practices were followed, e.g., simulations to predict loads on the parts, finite element analysis to predict stresses, and fatigue life calculation to predict the usage period under the nominal loading.

B. Leg Mechanism

In designing the leg mechanism, a special emphasis was given to actuator placement as it plays a major role in defining the leg inertia. Deploying the actuators around the hip reduces the leg inertia with respect to the hip joint. Hence, the system could imitate a pendulum in a more consistent manner, leading to energetically efficient motion patterns [26]. Furthermore, a leg with reduced inertia could lead to diminished swing

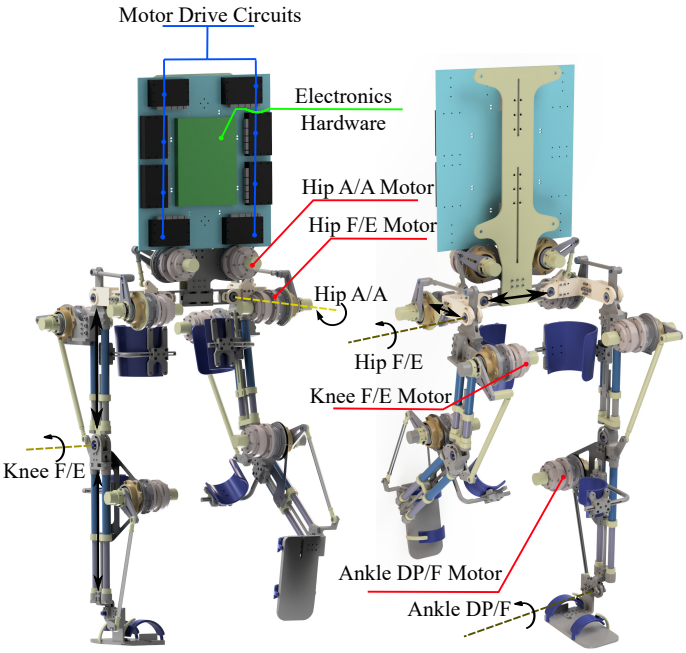


Fig. 2: Joint configurations of the exoskeleton Co-Ex.

leg dynamics, which can be advantageous when considering abstracted models for planning and control.

To this end, three distinct leg mechanisms could be considered; see Fig. 3: a) actuator-joint collocation, b) all actuators are bedded around the waist [29], c) hip and knee actuators are bedded around the waist, and ankle actuator was placed on the calf region. Using the CAD data, sagittal plane leg inertia with respect to the hip joint is computed as 4.727, 2.975, and 3.821 kgm^2 for mechanisms -a, -b, and -c, depicted with $\mathbb{M}_A$, $\mathbb{M}_B$, and $\mathbb{M}_C$, respectively. Therefore, $\mathbb{M}_B$ appears to be the most feasible option in terms of reducing leg inertia.

While $\mathbb{M}_B$ appears to be effective in reducing the leg inertia, transmitting ankle torque through the knee joint via a series of two 4-bars causes a kinematic loop between the ankle and knee joints. It hinders the independent control of joints and necessitates the use of an extra kinematic loop solver. Even if these disadvantages are leveraged through the solution of the kinematic loop and the selection of optimal 4-bar parameters, two issues persist: i) $\mathbb{M}_B$ greatly reduces the ankle joint range while increasing the knee joint torque demand, and ii) the use of two 4-bars in series leads to accumulated backlash.

For a comprehensive analysis, we conducted six groups (S1, S2, S3, S4, S5, S6) of dynamic walking simulations in which the robot model's legs were configured in accordance with $\mathbb{M}_A$, $\mathbb{M}_B$, and $\mathbb{M}_C$. In each group simulation study, all robot models were instructed to walk dynamically with eight distinct forward speeds: 0, 30, 60, 90, 120, 150, 180, and 210 mm/s. In S1, S2, and S3, the swing foot clearance was 40 mm. It was 60 mm in S4, S5, and S6. Single support periods were 0.5 s for S1 and S4, 0.6 s for S2 and S5, and 0.7 s for S3 and S6. Double support periods were 0.05 s for all simulation runs. We computed the total power consumption and indicated its rms value for all three leg configurations in

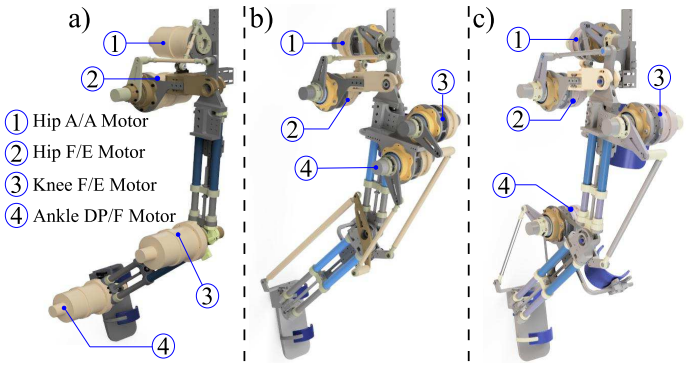


Fig. 3: Possible leg mechanisms. a) Motors are collocated at the respective joints: $\mathbb{M}_A$. b) All motors are gathered around the waist in which the ankle joint is actuated via two 4-bar mechanisms in series: $\mathbb{M}_B$. c) Hip and knee motors are gathered around the waist while ankle motors are located on the calf region: $\mathbb{M}_C$.

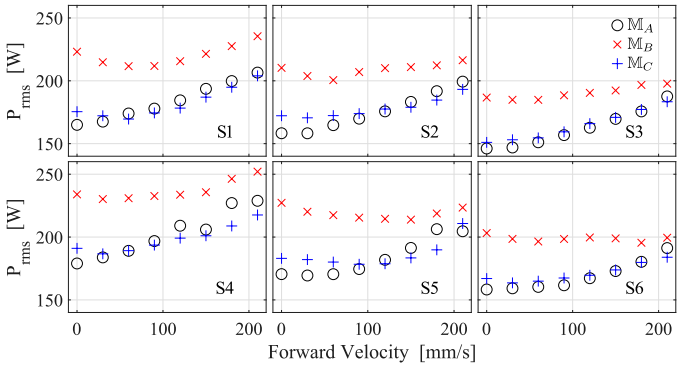


Fig. 4: Six groups of simulation runs were performed concerning all three leg configurations.

Fig. 4. As a result, we observe that $\mathbb{M}_B$ has a greater power requirement in all cases, whereas $\mathbb{M}_A$ and $\mathbb{M}_C$ have similar power requirements. Considering these results, $\mathbb{M}_C$ is deemed to be the most feasible option as it provides a leg configuration with reduced torque/power demand and inertia.

For further comparison, we conducted self-balancing squatting experiments in which *Co-Ex* legs were configured in accordance with $\mathbb{M}_B$ and $\mathbb{M}_C$. Fig. 5 displays actual torque measurements. As may be observed, $\mathbb{M}_B$ demands greater motor torque for the knee joint. This result indicates the feasibility of $\mathbb{M}_C$.

C. Human-Robot Connection

In order to connect a human limb to our exoskeleton, we use custom-built brace structures, which include straps and Velcro-like fasteners to ensure suitable don/doff procedures. These braces were designed in such a way that they transmit the forces along the desired axis of motion while they should not exert parasitic forces along the other axes [30].

To this end, we modeled the human limb fixation brace as shown in Fig. 6. Points H, K, and B indicate the exoskeleton hip joint, the exoskeleton knee joint, and the position of the

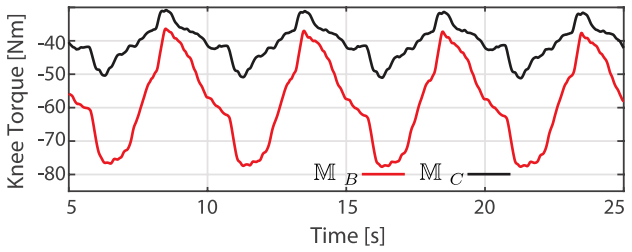


Fig. 5: Knee torque measurements from squatting experiments while using 2 distinct leg mechanisms.

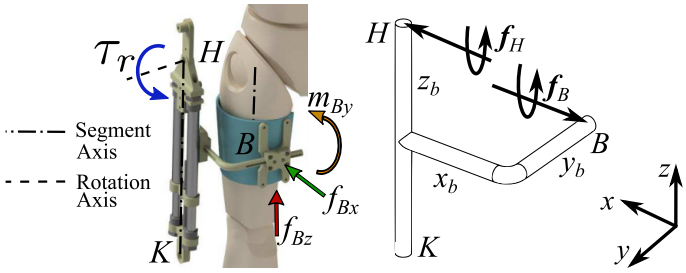


Fig. 6: Left: Connections between human limbs and Co-Ex are achieved via braces. Right: A free body diagram concerning the connection between Co-Ex and a human limb.

brace connection on the human thigh, respectively. The robot exerts torque τ_r at the point H along the F/E axis, which is also represented by the y axis. The symbols $\mathbf{f}_H \in \mathbb{R}^6$ and $\mathbf{f}_B \in \mathbb{R}^6$ denote the spatial force vectors acting on points H and B, respectively. Concerning the point i $(i = H, K, B)$, the spatial force vector is defined as $\mathbf{f}_i = [m_{ix}\ m_{iy}\ m_{iz}\ f_{ix}\ f_{iy}\ f_{iz}]^\intercal$. The parameters $(m_{ix},\ m_{iy},\ m_{iz})$ and $(f_{ix},\ f_{iy},\ f_{iz})$ symbolize the moments and translation forces along the x, y, and z directions, respectively. The vector $\mathbf{r_b} = [x_b\ y_b\ z_b]^\intercal$ represents the displacement vector, defined from point B to point H.

The reaction force at point H has three components along x, y, and z axes, while the reaction moment has only two components along x and z axes. The resulting internal forces and moments transmitted from the exoskeleton hip to the human thigh are computed as follows [31]:

$$\mathbf{f}_H = \begin{bmatrix} \mathbf{I_{3x3}} & -S(\mathbf{r_b}) \\ \mathbf{0_{3x3}} & \mathbf{I_{3x3}} \end{bmatrix} \mathbf{f}_B, \tag{1}$$

where $S(\mathbf{r_b})$ is the skew-symmetric form of the vector $\mathbf{r_b}$. $\mathbf{I_{3x3}}$ and $\mathbf{0_{3x3}}$ are unit and zero matrices. Using (1) and spatial vector notation, the robot joint torque τ_r can be expressed in terms of brace force components as follows:

$$\tau_r = m_{by} - f_{bx} z_b + f_{bz} x_b. \tag{2}$$

Considering (2), we draw the following conclusion to attain feasible force transmission from an exoskeleton to a human limb: i) The moment m_{by}, indicated by the orange arrow in Fig. 6, should be applied over a broad contact area between the human and the brace to avoid high stress, ii) the force f_{bx}, shown by the green arrow in Fig. 6, needs to be increased; yet the contact area should be large enough to reduce the applied pressure on the human body, and iii) the force f_{bz}, shown by the red arrow in Fig. 6, should be minimized to prevent hyperstatic forces that may act tangentially against the human skin.

Consequently, the braces were manufactured with a wide metal structure to avoid high stress. Moreover, soft materials, e.g., polypropylene, were used to provide comfort. The parameter z_b is selected to ensure ergonomic fixation, while x_b is set to zero to eliminate the undesirable vertical force f_{bz}. Although this analysis focused on the thigh brace, a similar analysis can be conducted for the calf brace.

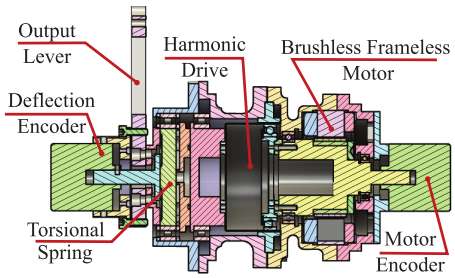


Fig. 7: Series elastic actuator unit, CAD model.

TABLE I: SEA Specifications

Parameter	Value
Maximum Angular Velocity (rpm)	44.09
Maximum Continuous Torque (Nm)	96
Mass (kg)	2.87
Radius x Length (mm x mm)	53.5 x 108
Stiffness (Nm/deg)	40
Torque Resolution (mNm)	3.90
Torque-to-mass Ratio (Nm/kg)	33.45

D. Actuation: Series Elasticity and Torque Controllability

The joints of the proposed exoskeleton are powered via series elastic actuator units built in-house. Each unit consists of a frameless and brushless motor (Kollmorgen TBM 7615A) and a strain wave gear (CPL-25A-100-2A2) with a ratio of 100:1. Actuator requirements, e.g., continuous torque demand, link side velocity, were determined via 3D walking simulations using a lumped model of our exoskeleton and a 90 kg human subject [32]. A custom-built torsional spring with a stiffness value of 80 Nm/deg was placed between the gear output and link [33]. The spring topology was optimized for size reduction while guaranteeing a calculated fatigue life of approximately 4.3 years for continuous operation. Two absolute encoders with 23-bit resolution (Broadcom Avago AS38 H39ES135) were employed to measure motor angle and spring deflection separately. Table I tabulates the main properties of the unit. The CAD figure can be viewed in Fig. 7. Refer to [33] for details.

E. Electronics and Communication

The general block diagram concerning the electronics hardware is depicted in Fig. 8. As the main controller, we employed a computer that possesses an Intel Core i5 microprocessor and 8 GB RAM. To yield real-time operations, Ubuntu 18.04 with

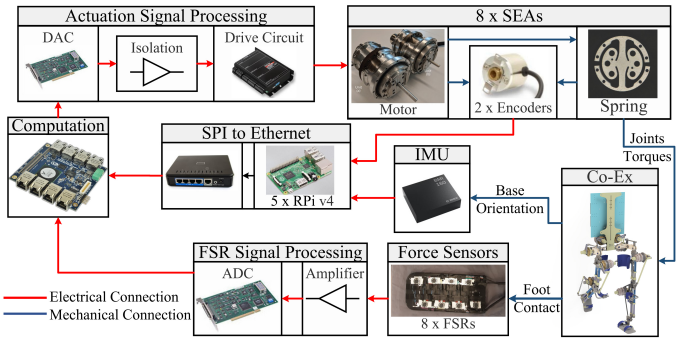


Fig. 8: Electronic hardware of Co-Ex.

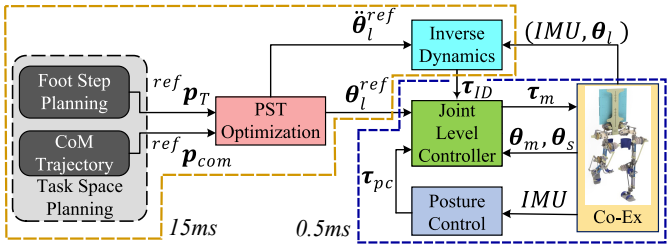


Fig. 9: Locomotion control framework.

the Xenomai RTOS (Real-time Operating System) patch was integrated. As a result, a deterministic sampling frequency of 2.0 kHz was yielded, and the average variance in the sampling period was less than 5%. The actuators were commanded using Maxon ESCON 70/10 motor drives. Command signals were generated using Advantech's PCI-1723 D/A converter, which has 16-bit resolution.

As described in subsection II-D, each joint has two high-resolution encoders (16 encoders in total), and each encoder provides 40-bit-long (23-bit angle data, 16-bit multiturn data, 1-bit error) information in each cycle. In order to collect such data, we constructed a custom-built Ethernet network on the backpack of the robot. The encoders communicate via SSI (Synchronous Serial Interface). We utilized one RPi-4B (Raspberry Pi) for four encoders, making it 4 RPis in total for 16 encoders. Each RPi can receive data from 4 SPI devices in parallel. RPis were docked on a custom-made daughter board to facilitate SPI (Serial Peripheral Interface) connections by converting SSI signals to SPI with the help of differential line drivers. RPis were run on EVL RTOS. To achieve high-speed/low-latency encoder data acquisition (40-bits@1.25 Mhz), DMAs (Direct Memory Access) were enabled for 4 SPI interfaces on RPis. All 4 RPi units were connected to the host computer via Ethernet with a switcher placed on the exoskeleton.

To measure orientation and acceleration, an IMU (BMI160, Bosch Sensortec) unit was placed at the pelvis. Another RPi was used to collect IMU data via SPI, and it is linked to the host computer via Ethernet. To measure GRF (Ground Reaction Force) and ZMP (Zero Moment Point), 8 distributed force sensing elements (Interlink FSR UX 402) were deployed under each foot sole [34]. Force data was amplified, preprocessed, and linked to the main controller via Advantech's PCI-1716 A/D converter, which has 16-bit resolution.

III. Controller Synthesis

The proposed control framework is displayed in Fig. 9 and it was constructed to ensure Co-Ex exhibits the desired locomotion behavior. In this figure, the parameters ${}^{ref}\mathbf{p}_T \in \mathbb{R}^{12}$ and ${}^{ref}\mathbf{p}_{com} \in \mathbb{R}^3$ denote the reference Cartesian displacements of the feet and CoM, respectively. $\boldsymbol{\theta}_l \in \mathbb{R}^{nr}$, $\boldsymbol{\theta}_m \in \mathbb{R}^{nr}$, and $\boldsymbol{\tau}_m \in \mathbb{R}^{nr}$ indicate the link side (subscript $_l$) and motor side (subscript $_m$) position and torque, respectively. The number of actuated robot joints is represented with nr. $\boldsymbol{\theta}_s \in \mathbb{R}^{nr}$ stands for spring deflection angle. The superscript ref symbolizes the reference value. The vectors $\boldsymbol{\tau}_{ID} \in \mathbb{R}^{nr}$ and $\boldsymbol{\tau}_{pc} \in \mathbb{R}^{nr}$ refer to the inverse dynamics and posture control torques, respectively.

This framework operates at two levels. The high-level controller, running at 66.67 Hz, is responsible for task-space planning through the generation of feasible Cartesian trajectories. It also handles the computation of optimization-based inverse kinematic algorithm and inverse dynamics algorithm. The low-level controller, running at 2 kHz, handles joint-level control, posture control, and the execution of interface instructions with the Co-Ex electronics platform. Both controllers are simultaneously executed in real-time.

A. Task Space Planning

The main duty of the Task Space Planning block is to generate feasible CoM and feet trajectories considering the contact phases. To this end, we utilized the analytical trajectory generator proposed in [35]. This ZMP-based trajectory generator ensures the continuity of the CoM trajectories in the acceleration level regardless of the contact phase and automatically arranges boundary conditions for smooth joint patterns to prevent sudden torque jumps. Refer to [35] for details.

B. Prioritized Stack of Task (PST) Optimization

Due to the underactuated nature of the Co-Ex legs, it is not viable to develop an inverse kinematic solution that achieves all the desired Cartesian constraints. An alternative approach is to minimize the norm of residuals between the desired and generated Cartesian trajectories as follows:

$$\dot{\mathbf{q}}^* = \arg\min_{\forall \dot{\mathbf{q}} \in \mathbb{R}^d} ||\dot{\mathbf{p}}^{ref} - \mathbf{J}(\mathbf{q})\dot{\mathbf{q}}||^2. \tag{3}$$

In (3), $\dot{\mathbf{p}}^{ref} = [{}^{ref}\dot{\mathbf{p}}_T^\intercal \ \mathbf{0}_{1\times 3} \ {}^{ref}\dot{\mathbf{p}}_{com}^\intercal]^\intercal$. The matrix $\mathbf{J}(\mathbf{q}) \in \mathbb{R}^{18\times d}$ denotes the robot Jacobian matrix that maps Cartesian velocities to joint velocities; d is the number of degrees of freedom. The vector $\dot{\mathbf{q}} \in \mathbb{R}^d$ represents the joint velocity vector.

In this regard, relying solely on (3) could result in infeasible solutions that violate high-priority constraints, e.g., CoM trajectory. Therefore, a PST optimization algorithm is employed where low-priority constraints, such as swing foot orientation, are resolved without disrupting high-priority constraints. This prioritization is achieved by solving a sequence of constrained

least-square optimization problems. The higher-priority constraints are imposed on the lower-priority ones in the form of equality constraints. Thus, the optimization problem (3) is reformulated as follows:

$$\overline{\mathbf{q}}^* = \arg\min_{\forall \overline{\mathbf{q}} \in R^{2d}} \left\| \overline{\mathbf{p}}_p - \overline{\mathbf{J}}_p \overline{\mathbf{q}} \right\|^2 \quad (4)$$

$$s/t \quad \left[\overline{\mathbf{J}}_{p-1}^\intercal \ \overline{\mathbf{J}}_{p-2}^\intercal \ \cdots \ \overline{\mathbf{J}}_1^\intercal\right]^\intercal \overline{\mathbf{q}} = \left[\overline{\mathbf{p}}_{p-1}^\intercal \ \overline{\mathbf{p}}_{p-2}^\intercal \ \cdots \ \overline{\mathbf{p}}_1^\intercal\right]^\intercal . \quad (5)$$

In eqs. (4) and (5), $\overline{\mathbf{q}}$, $\overline{\mathbf{p}}_p$, and $\overline{\mathbf{J}}_p$ are defined as follows:

$$\overline{\mathbf{q}} = \begin{bmatrix} \dot{\mathbf{q}} \\ \ddot{\mathbf{q}} \end{bmatrix}, \ \overline{\mathbf{p}}_p = \begin{bmatrix} \dot{\mathbf{p}}^{ref} \\ \ddot{\mathbf{p}}^{ref} \end{bmatrix}_p, \ \overline{\mathbf{J}}_p = \begin{bmatrix} \mathbf{J}(\mathbf{q}) & \mathbf{0} \\ \dot{\mathbf{J}}(\mathbf{q}) & \mathbf{J}(\mathbf{q}) \end{bmatrix}_p, \quad (6)$$

where the subscript p indicates the prioritization level. Eq. (4) provides optimized joint trajectories at the velocity and acceleration levels, enabling seamless integration with the inverse dynamics block. The optimal joint displacement vector is computed for each sample as $\mathbf{q}_k^* = \mathbf{q}_{k-1}^* + t_s \dot{\mathbf{q}}_k^* + 0.5 t_s^2 \ddot{\mathbf{q}}_k^*$, where the subscript k and symbol t_s refer to the sampling index and time, respectively. The reference displacement vector $\boldsymbol{\theta}_l^{ref} = \mathbf{S}\mathbf{q}^*$ is derived by selecting the actuated robot joints using the selection matrix $\mathbf{S} \in \mathbb{R}^{nr \times d}$.

C. Inverse Dynamics

The inverse dynamics is used in the sense of computed torque control such that it improves compliance and joint trajectory tracking. Unlike manipulator arms, our exoskeleton has no fixed base. Therefore, the dynamics of a floating-base system is considered [31], [36]:

$$\mathbf{H}(\mathbf{q})\ddot{\mathbf{q}} + \mathbf{C}(\mathbf{q}, \dot{\mathbf{q}})\dot{\mathbf{q}} + \mathbf{G}(\mathbf{q}) = \mathbf{S}^\intercal \boldsymbol{\tau} + \mathbf{J}_\mathbf{c}(\mathbf{q})^\intercal \boldsymbol{\lambda}_c, \quad (7)$$

where $\boldsymbol{\tau}$ represents the joint torque vector, $\boldsymbol{q}$ denotes the joint position vector including floating base parameters, $\mathbf{H}(\mathbf{q}) \in \mathbb{R}^{d \times d}$ is the inertia matrix, $\mathbf{C}(\mathbf{q}, \dot{\mathbf{q}}) \in \mathbb{R}^{d \times d}$ is the Coriolis and centrifugal matrix, $\mathbf{G}(\mathbf{q}) \in \mathbb{R}^d$ stands for the gravitational terms, nc is the number of contact bodies, and $\boldsymbol{\lambda}_c \in \mathbb{R}^{6nc \times 1}$ is the vector storing spatial forces at contacts. For multiple contacts, $\boldsymbol{\lambda}_c$ is expressed as $\boldsymbol{\lambda}_c = [{}^1\boldsymbol{\lambda}_c^\intercal \ {}^2\boldsymbol{\lambda}_c^\intercal \ \cdots \ {}^{nc}\boldsymbol{\lambda}_c^\intercal]^\intercal$. The symbol $\mathbf{J}_c(\mathbf{q}) \in \mathbb{R}^{6nc \times d}$ represents the Jacobian matrix concerning the contact frames. The floating base model in (7) can be decomposed as follows:

$$\mathbf{H}_{fb}(\mathbf{q})\ddot{\mathbf{q}} + \mathbf{C}_{fb}(\mathbf{q}, \dot{\mathbf{q}})\dot{\mathbf{q}} + \mathbf{G}_{fb}(\mathbf{q}) = \mathbf{J}_{c,fb}(\mathbf{q})^\intercal \boldsymbol{\lambda}_c, \quad (8)$$

$$\mathbf{H}_r(\mathbf{q})\ddot{\mathbf{q}} + \mathbf{C}_r(\mathbf{q}, \dot{\mathbf{q}})\dot{\mathbf{q}} + \mathbf{G}_r(\mathbf{q}) = \boldsymbol{\tau}_{ID} + \mathbf{J}_{c,r}(\mathbf{q})^\intercal \boldsymbol{\lambda}_c. \quad (9)$$

In eqs. (8)-(9), $\mathbf{H}_{fb}(\mathbf{q}), \mathbf{C}_{fb}(\mathbf{q}, \dot{\mathbf{q}}), \mathbf{G}_{fb}(\mathbf{q}), \mathbf{J}_{c,fb}(\mathbf{q})$ represent the top six rows of $\mathbf{H}(\mathbf{q}), \mathbf{C}(\mathbf{q}, \dot{\mathbf{q}}), \mathbf{G}(\mathbf{q}), \mathbf{J}_c(\mathbf{q})$, corresponding to the floating base joints. The matrices $\mathbf{H}_r(\mathbf{q}), \mathbf{C}_r(\mathbf{q}, \dot{\mathbf{q}}), \mathbf{G}_r(\mathbf{q}), \mathbf{J}_{c,r}(\mathbf{q})$ represent the bottom nr rows of $\mathbf{H}(\mathbf{q}), \mathbf{C}(\mathbf{q}, \dot{\mathbf{q}}), \mathbf{G}(\mathbf{q}), \mathbf{J}_c(\mathbf{q})$, corresponding to the actuated robot joints.

The inverse dynamics approach involves two steps. The first step computes $\boldsymbol{\lambda}_c$ using (8). The second step uses the obtained $\boldsymbol{\lambda}_c$ to compute $\boldsymbol{\tau}_{ID}$ via (9). For SSP (Single Support Phase), the resolution of (8) is performed as follows: $\lambda_c = (\mathbf{J}_{c,fb}(\mathbf{q})^\intercal)^{-1}(\mathbf{H}_{fb}(\mathbf{q})\ddot{\mathbf{q}} + \mathbf{C}_{fb}(\mathbf{q}, \dot{\mathbf{q}})\dot{\mathbf{q}} + \mathbf{G}_{fb}(\mathbf{q}))$. For the case of DSP (Double Support Phase), no unique solution exists due to contact force redundancy. This leads to the use of pseudo-inverse as follows: $\lambda_c = (\mathbf{J}_{c,fb}(\mathbf{q})^\intercal)^\dagger(\mathbf{H}_{fb}(\mathbf{q})\ddot{\mathbf{q}} + \mathbf{C}_{fb}(\mathbf{q}, \dot{\mathbf{q}})\dot{\mathbf{q}} + \mathbf{G}_{fb}(\mathbf{q}))$, where the superscript † denotes the pseudo-inverse.

D. Posture Control

To ensure dynamic balance despite external perturbations, a posture control algorithm was developed. To this end, the error in floating base orientation velocity is computed as follows:

$$\boldsymbol{\omega}_{fb}^{error} = \boldsymbol{\omega}_{fb}^{ref} - \boldsymbol{\omega}_{fb}^{act}, \quad (10)$$

where $\boldsymbol{\omega}_{fb}^{ref} \in \mathbb{R}^3$ and $\boldsymbol{\omega}_{fb}^{act} \in \mathbb{R}^3$ denote the reference and measured floating base orientation velocity values, respectively. The error $\boldsymbol{\omega}_{fb}^{error}$ can be projected onto the contact body coordinate frame using the following expression:

$$\boldsymbol{\lambda}_c^{pc} = ((\mathbf{J}_{c,fb}(\mathbf{q})\mathbf{S}_{or})^\intercal)^\dagger \mathbf{K}_{pc} \boldsymbol{\omega}_{fb}^{error}. \quad (11)$$

The parameter $\boldsymbol{\lambda}_c^{pc}$ represents the projection of $\mathbf{K}_{pc}\boldsymbol{\omega}_{fb}^{error}$ onto the contact body coordinate frame. $\mathbf{S}_{or} \in \mathbb{R}^{6 \times 3}$ is a selection matrix to keep the necessary columns of the Jacobian matrix that correspond to the floating base angular velocity. The matrix $\mathbf{K}_{pc} \in \mathbb{R}^{3 \times 3}$ is a diagonal positive semi-definite gain matrix. The error could be mapped to joint torques as $\boldsymbol{\tau}_{pc} = \mathbf{J}_{c,r}(\mathbf{q})^\intercal \boldsymbol{\lambda}_c^{pc}$. Accordingly, the control law for the posture control can be yielded as follows:

$$\boldsymbol{\tau}_{cmd} = \boldsymbol{\tau}_{pc} + \boldsymbol{\tau}_{ID} + \boldsymbol{\tau}_s^{ref}, \quad (12)$$

where $\boldsymbol{\tau}_s^{ref}$ represents the SEA spring reference torque; see the subsection III-E.

E. Joint-level control

The joint-level controller has two modes to accommodate various tasks: i) position control mode and ii) torque control mode. The position controller was built on top of the torque controller. Thus, the performance of the torque controller has pivotal importance. Furthermore, one can configure the controller in torque control mode simply by deactivating the outer position control loop. In order to ensure high-fidelity torque control performance, we used a cascaded controller method with a disturbance observer, which exhibited superior performance over the existing methods [37], [38]; see Fig. 10. In this figure, τ_s, K_s, τ_{ff}, τ_{ID}, τ_{pc}, θ_m, and θ_l denote the spring torque, spring stiffness, feedforward torque, inverse dynamics torque, posture controller output, motor angle, and link angle, respectively. In this controller, the nominal transfer function for the SEA model, P_n, defines the relationship between spring deflection θ_s and motor torque τ_m [38]:

$$P_n(s) = \frac{P_{mn}(s)N^{-1}}{1 + K_s P_{mn}(s)N^{-2} + K_s P_{ln}(s)} \quad (13)$$

In (13), s is the Laplace variable, and N is the gear ratio. P_{mn} and P_{ln} are the nominal motor and link model; $P_{mn}(s) = 1/(s^2 J_{mn} + s b_{mn})$ and $P_{ln}(s) = 1/(s^2 J_{ln} + s b_{ln})$. J_{mn}, b_{mn} and J_{ln}, b_{ln} respectively denote nominal motor inertia and viscous friction coefficients for P_{mn} and P_{ln}. Q_2 is a second-order low-pass filter.

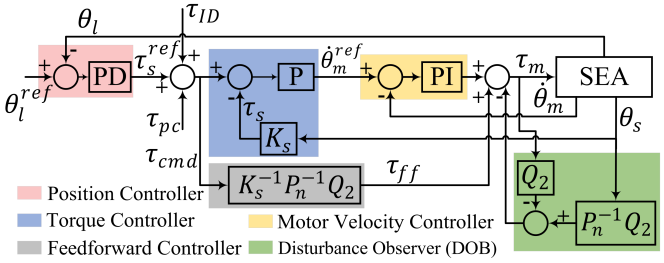


Fig. 10: Joint-level control block diagram. Robot joints can be purely force controlled if the outer-loop position control is deactivated.

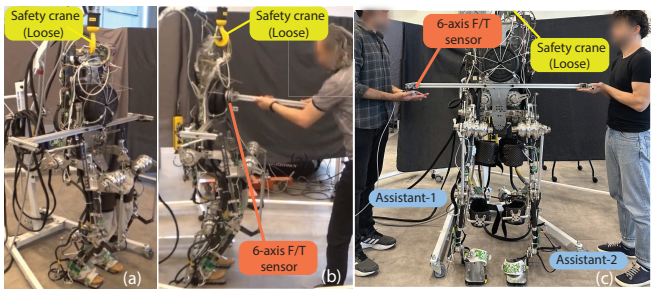


Fig. 11: In all experiments, a safety crane was used but kept loose. a) In squatting and swaying experiments the robot maintained its own balance in 3D. b) In push recovery experiments, the robot was hit via a rod with a 6-axis F/T sensor at its tip. The robot also maintained its own balance in 3D. c) In walking experiments, two assistants provided support along the coronal plane to emulate the effect of crutch use. A 6-axis F/T sensor was used to quantify human assistance during walking. See the multimedia attachment.

IV. Experiment Results

Currently, the existing protocols for robot-aided walking focus on quasi-static gaits [39]. There is a protocol for dynamic walking for the fully actuated exoskeleton Atalante [11]. These protocols could not be fully adapted due to structural differences concerning the dynamic walking support with an underactuated exoskeleton.

In light of this, we conducted experiments using a dummy manikin with passive joints and dummy upper body weights to verify the self-stabilization and locomotion capabilities of our exoskeleton prototype Co-Ex. The leg length of the dummy manikin is 94 cm. Disturbance attenuation, squatting, and swaying experiments were conducted while the robot maintained its own balance; see Fig. 11-(a) and -(b). However, due to the inherent flexibility of exoskeletons [27], quasi-static and dynamic walking experiments were conducted with a lateral boom where two people provide support along the coronal plane; see Fig. 11-(c). In this setting, a possible use of crutches was emulated by the two people. Using a 6-axis force sensor (OnRobot, HEX), the human contribution was collected for quantifiable assessment. Furthermore, disturbance attenuation experiments were repeated with a 55 kg dummy manikin to emulate the effects of an able-bodied user.

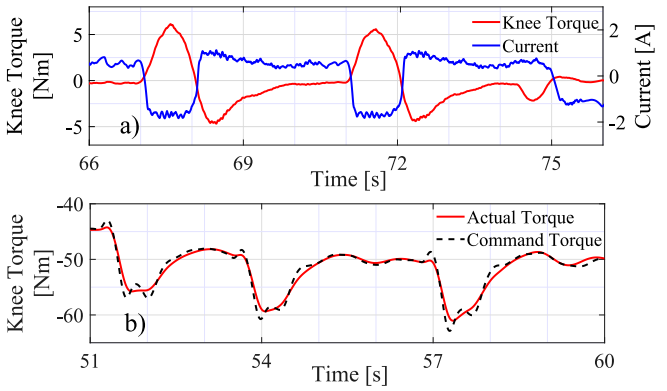


Fig. 12: a) Zero torque control for transparency. b) Joint-level torque tracking performance.

A. Joint-Level Torque Control

Two experiments were conducted to verify the torque control performance. In the first experiment, zero torque reference was applied to check transparency. The shank was manually moved up such that the knee joint rotated from 0^o to -28^o and then released. Fig. 12.a displays the results where solid blue and red lines stand for the motor current command and measured torque, respectively. A phase difference of 180^o indicates that the controller counteracts to render backdrivability despite friction.

In normal operation, joint-level torque control serves as an inner-loop controller; see Figs. 9 and 10. Thus, its performance was also verified during a push-recovery experiment. Fig. 12.b displays both the torque command (dashed black) produced by the outer loop posture controller and the actual torque (solid red). It was observed that the torque controller exhibited a sufficient tracking performance, as the RMS of the tracking error was 1.4 Nm. This is only 2.5% of the reference trajectory's RMS value.

B. Disturbance Attenuation Capability

A set of experiments were conducted to test the push recovery ability when there are external perturbations. To this end, external forces were manually applied to the robot via a sensorized rod; see Fig. 11-(b).

1) Push Recovery through Sagittal Plane: Fig. 13 depicts the results concerning the push-recovery along the sagittal plane when using a light and heavier dummy. Three consecutive external forces (F_{ext}) were applied. Examining Fig. 13, one can observe that the robot maintained balance as the pitch axis torso angular velocity (ω_y) and x-axis ZMP (x_{zmp}) were well regulated [40]. Moreover, the joint-level torque controller showed favorable tracking performance.

To illustrate the effectiveness of our controller over the conventional approach, we conducted additional experiments; see Fig. 14. The conventional controller is based on center of mass regulation via impedance control [41]. In this comparison, the robot was subject to external forces along the sagittal axis

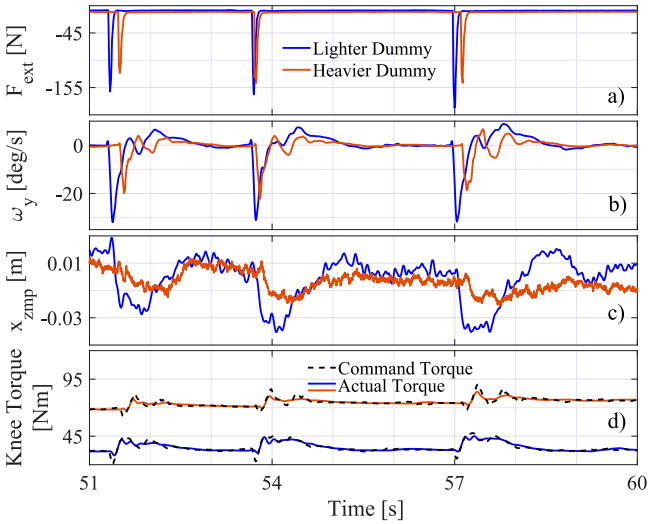


Fig. 13: a) Three consecutive perturbations F_{ext} along the sagittal plane. b) Pitch axis torso angular velocity. c) ZMP response along the x-axis. d) Joint-level torque tracking performance.

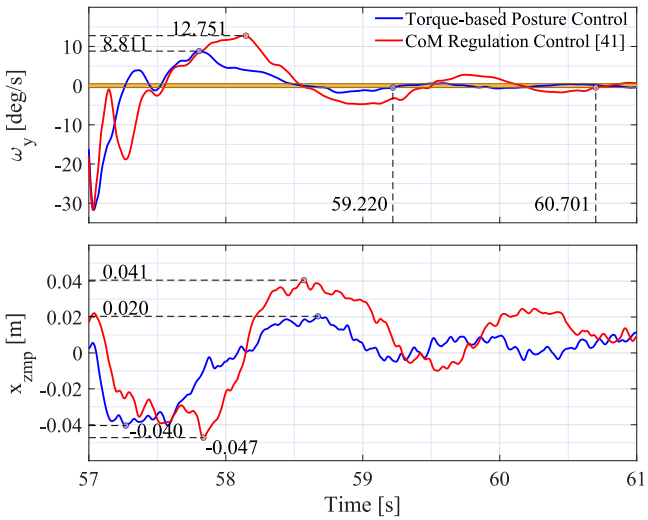


Fig. 14: Posture control comparison. Top: Pitch axis torso angular velocity. Bottom: ZMP response along the x-axis.

with amplitudes of 196.3 N (led to an impulse of 111.2 Ns) and 192.6 N (led to an impulse of 110.6 Ns), when it was controlled via the proposed posture controller and conventional controller, respectively. In the figure, solid blue and red lines indicate the responses of the proposed and conventional controllers. The orange shaded area depicts the $\pm 5\%$ settling region. As a result, both controllers showed recovery, yet the proposed torque-based posture control provided 31% reduction in peak-to-peak value and 1.5 s less settling time concerning ω_y response. Likewise, the peak-to-peak value of x_{zmp} is 32% less when the proposed controller is applied. In light of this experiment, we assessed that the proposed controller could significantly improve the robot's disturbance attenuation capability. Note that this comparison was not conducted for the case of heavy dummy manikin as the conventional controller could not stabilize the system; see the multimedia attachment.

2) Push Recovery through Coronal Plane: A similar set of push recovery experiments was conducted in which external forces were applied through the coronal plane; see Fig. 15. As a result, the robot was able to withstand external pushes since the controller successfully regulated roll axis torso angular velocity (ω_x) and y-axis ZMP (y_{zmp}) [40]. Similarly, torque tracking at the joint level was sufficient.

C. Self-Balancing Squatting and Swaying

In robot-aided rehabilitation, squatting and swaying movements are used [3]. Therefore, we experimentally verified the squatting and swaying capabilities of the robot. A sine wave with a frequency of 0.5 Hz was used to generate trajectories. The results can be viewed in Fig. 16 and Fig. 17.

Trajectory tracking results are displayed in Fig. 16, where solid red and dashed black lines indicate actual and reference trajectories of the pelvis. Actual pelvis trajectories were estimated using the method reported in [36]. The tracking error is represented with solid blue lines. Examining this figure,

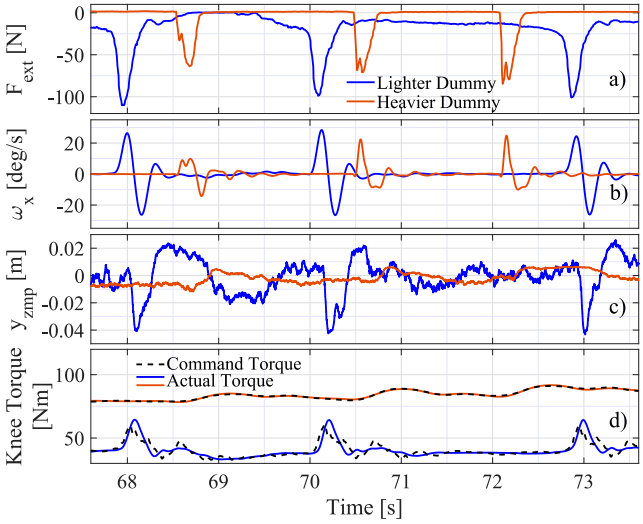


Fig. 15: a) Three consecutive perturbations F_{ext} along the coronal plane. b) Roll axis torso angular velocity. c) ZMP response along the y-axis. d) Joint-level torque tracking performance.

we observe that the trajectory tracking is sufficient for the target squatting and swaying tasks. The maximum absolute errors are 1.1 mm and 6.7 mm for squatting and swaying, respectively. Furthermore, ZMP measurements are plotted in Fig. 17. In both experiments, ZMP measurements stayed within the support polygon, thereby indicating the dynamic balance of the system [40].

D. Walking Locomotion Capability

To verify the locomotion capability of the system, we conducted walking experiments where two distinct gait patterns were used: i) quasi-static, and ii) dynamic.

1) Quasi-Static Walking: In these experiments, the average forward velocity was set to 5 cm/s, the single and double

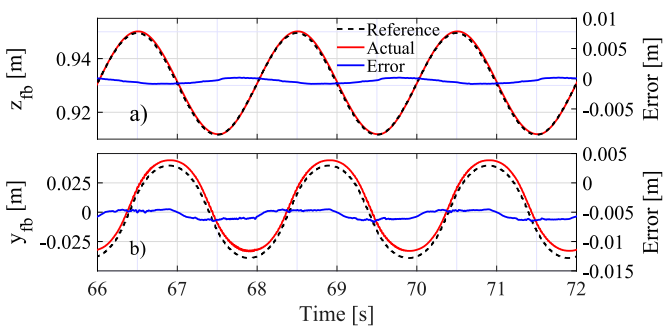


Fig. 16: a) Vertical pelvis position tracking for squatting. b) Lateral pelvis position tracking for swaying.

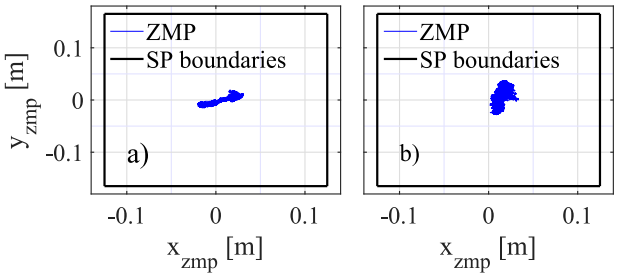


Fig. 17: ZMP responses: a) squatting, b) swaying, shown in the solid blue line. Support polygon (SP) boundaries are shown in a solid black line.

support phase periods were 1 s, and the maximum foot clearance was 6 cm. In this walking mode, the mean forward velocity was kept relatively low to avoid balancing issues. Fig. 18.a depicts the tracking result of the forward displacement of pelvis x_{fb}. The actual, reference, and error values are shown in solid red, black dashed, and solid blue lines, respectively. As the result, the robot was able to perform quasi-static gait in which the RMS of the tracking error was 5.48 cm.

2) Dynamic Walking: In dynamic walking experiments, the average forward velocity was set to 10 cm/s, the single and double support phase periods were 0.8 s and 0.2 s, and the maximum foot clearance was 6 cm. Fig. 18.b depicts the tracking result of the forward displacement of pelvis x_{fb}. The actual, reference, and error values are shown in solid red, black dashed, and solid blue lines, respectively. As the result, the robot was able to perform dynamic walking in which the RMS of the tracking error was 5.35 cm.

3) Dynamic Walking Effects on Human-Robot Interaction: To investigate the advantage of dynamic walking over quasi-static walk in terms of reduced human effort, we conducted a set of experiments in which the robot performed 30 steps in both modes. We focused our assessment on sagittal plane force magnitude ($f_{sag} = \sqrt{f_x^2 + f_z^2}$) and moment ($m_y$), as they play a pivotal role in forward walking. Fig. 19 depicts the variations in the mean value of f_{sag} and m_y, in relation to SD (Standard Deviation): $\mu \pm 1 \cdot \sigma$. Examining this figure, we observe a 13% reduction in force magnitude along the sagittal plane. Furthermore, there is a significant decrease of 70% in

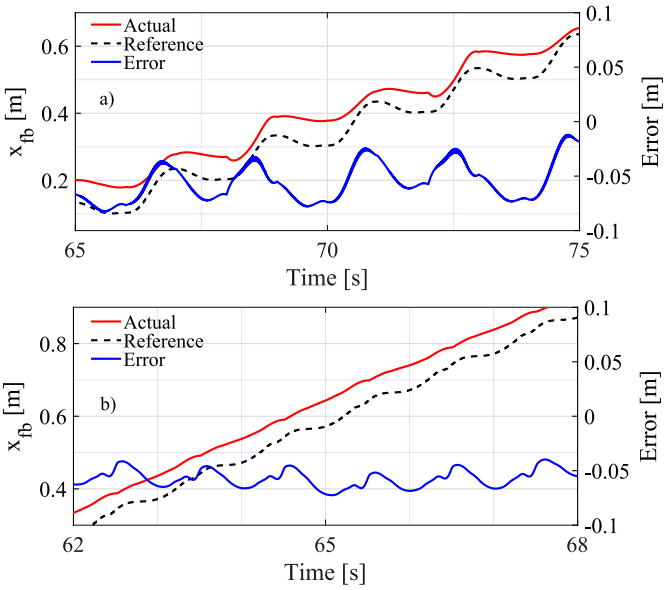


Fig. 18: a) x-axis pelvis position tracking for quasi-static walk. b) x-axis pelvis position tracking for dynamic walking.

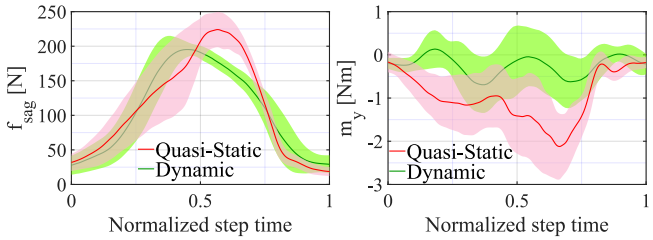


Fig. 19: Quasi-static walk vs dynamic walk. Left: force magnitude along the sagittal plane. Right: pitch axis moment.

interaction moment along the same plane. In light of this data, we argue that the dynamic walking capability of Co-Ex may reduce the upper body effort during a robot-aided walking scenario with crutches, as the required interaction forces were significantly contained.

V. Discussion and Conclusion

In this article, we presented the design, development, and control implementation procedures for the self-stabilizing bipedal exoskeleton Co-Ex. By effectively analyzing different leg mechanisms, a mechanical structure was constructed with reduced leg inertia and power consumption features. Co-Ex is capable of rejecting disturbance to maintain its balance in 3D, which may be crucial in robot-aided rehabilitation tasks, e.g., sit-to-stand. Co-Ex can also provide quasi-static and dynamic walking modes. An extensive set of experiment results verified the usability of the system as a proof of concept. Furthermore, it was demonstrated that dynamic walking mode, which is lacking in most state-of-the-art exoskeletons, could be efficient in decreasing the required user effort.

While the proposed prototype could perform target tasks, the unavoidable low structural stiffness due to wearability [27] led to tracking errors during walking experiments. To remedy

this issue, we are working on new dynamic models that take structural flexibility into account.

In this study, experiments were conducted using a dummy manikin with movement capabilities mirroring those of the target demographic. While the results could sufficiently indicate the functionality, the actual performance of the system should be tested with humans. To address this limitation, we are working toward the necessary experiment protocols that involve humans while the underactuated exoskeleton Co-Ex is in dynamic walking mode. Accordingly, we will report the human-involved experiments in our future work.

ACKNOWLEDGMENT

This work was supported by TÜBİTAK (The Scientific and Technological Research Council of Türkiye), Project Number 215E138.

REFERENCES

[1] R. Riener, "The cybathlon promotes the development of assistive technology for people with physical disabilities," *J. of NeuroEngineering and Rehabil.*, vol. 13, no. 1, May 2016.

[2] V. Lajeunesse, C. Vincent, F. Routhier, E. Careau, and F. Michaud, "Exoskeletons' design and usefulness evidence according to a systematic review of lower limb exoskeletons used for functional mobility by people with spinal cord injury," *Disability and Rehabil.: Assistive Technol.*, vol. 11, no. 7, pp. 535–547, Sep. 2015.

[3] L. Miller, A. Zimmermann, and W. Herbert, "Clinical effectiveness and safety of powered exoskeleton-assisted walking in patients with spinal cord injury: systematic review with meta-analysis," *Medical Devices: Evidence and Res.*, p. 455, Mar. 2016.

[4] J. Babič et al., "Challenges and solutions for application and wider adoption of wearable robots," *Wearable Technologies*, vol. 2, 2021.

[5] H. Li, D. Sui, H. Ju, Y. An, J. Zhao, and Y. Zhu, "Mechanical compliance and dynamic load isolation design of lower limb exoskeleton for locomotion assistance," *IEEE/ASME Trans. Mechatronics*, vol. 27, no. 6, pp. 5392–5402, Dec. 2022.

[6] Z. Chen, Q. Guo, T. Li, and Y. Yan, "Output constrained control of lower limb exoskeleton based on knee motion probabilistic model with finite-time extended state observer," *IEEE/ASME Trans. Mechatronics*, vol. 28, no. 4, pp. 2305–2316, Aug. 2023.

[7] L. Bergmann et al., "Lower limb exoskeleton with compliant actuators: Design, modeling, and human torque estimation," *IEEE/ASME Trans. Mechatronics*, vol. 28, no. 2, pp. 758–769, Apr. 2023.

[8] B. Ugurlu, H. Oshima, E. Sariyildiz, T. Narikiyo, and J. Babic, "Active compliance control reduces upper body effort in exoskeleton-supported walking," *IEEE Trans. on Human-Mach. Syst.*, vol. 50, no. 2, pp. 144–153, Apr. 2020.

[9] L. L. Haubert, D. D. Gutierrez, C. J. Newsam, J. K. Gronley, S. J. Mulroy, and J. Perry, "A comparison of shoulder joint forces during ambulation with crutches versus a walker in persons with incomplete spinal cord injury," *Archives of Physical Med. and Rehabil.*, vol. 87, no. 1, pp. 63–70, Jan. 2006.

[10] A. Rodríguez-Fernández, J. Lobo-Prat, and J. M. Font-Llagunes, "Systematic review on wearable lower-limb exoskeletons for gait training in neuromuscular impairments," *J. of NeuroEngineering and Rehabil.*, vol. 18, no. 1, Feb. 2021.

[11] J. Kerdraon et al., "Evaluation of safety and performance of the self balancing walking system Atalante in patients with complete motor spinal cord injury," *Spinal Cord Ser. and Cases*, vol. 7, 2021.

[12] M. C. Hoch, G. S. Staton, and P. O. McKeon, "Dorsiflexion range of motion significantly influences dynamic balance," *J. of Sci. and Med. in Sport*, vol. 14, no. 1, pp. 90–92, Jan. 2011.

[13] M. Bortole et al., "The h2 robotic exoskeleton for gait rehabilitation after stroke: early findings from a clinical study," *J. of NeuroEngineering and Rehabil.*, vol. 12, no. 1, Jun. 2015.

[14] R. Griffin et al., "Stepping forward with exoskeletons: Team IHMC's design and approach in the 2016 Cybathlon," *IEEE Robot. Autom. Mag*, vol. 24, no. 4, pp. 66–74, Dec. 2017.

[15] B. Ugurlu et al., "Variable ankle stiffness improves balance control: Experiments on a bipedal exoskeleton," *IEEE/ASME Trans. Mechatronics*, vol. 21, no. 1, pp. 79–87, Feb. 2016.

[16] L. Stickler, M. Finley, and H. Gulgin, "Relationship between hip and core strength and frontal plane alignment during a single leg squat," *Physical Therapy in Sport*, vol. 16, no. 1, pp. 66–71, Feb. 2015.

[17] B. K. Krautwurst, S. I. Wolf, D. W. Heitzmann, S. Gantz, F. Braatz, and T. Dreher, "The influence of hip abductor weakness on frontal plane motion of the trunk and pelvis in patients with cerebral palsy," *Res. in Develop. Disabilities*, vol. 34, no. 4, pp. 1198–1203, Apr. 2013.

[18] M. M. van der Krogt, S. L. Delp, and M. H. Schwartz, "How robust is human gait to muscle weakness?" *Gait & Posture*, vol. 36, no. 1, pp. 113–119, May 2012.

[19] C. F. Geiser, K. M. O'Connor, and J. E. Eearl, "Effects of isolated hip abductor fatigue on frontal plane knee mechanics," *Med. & Sci. in Sports & Exercise*, vol. 42, no. 3, pp. 535–545, Mar. 2010.

[20] C. Meijneke et al., "Symbitron exoskeleton: Design, control, and evaluation of a modular exoskeleton for incomplete and complete spinal cord injured individuals," *IEEE Trans. Neural Syst. Rehabil. Eng*, vol. 29, pp. 330–339, 2021.

[21] G. Barbareschi, R. Richards, M. Thornton, T. Carlson, and C. Holloway, "Statically vs dynamically balanced gait: Analysis of a robotic exoskeleton compared with a human," in *Proc 2015 37th Annu. Int. Conf. IEEE Eng. in Med. and Biol. Soc. (EMBC)*. IEEE, Aug. 2015, pp. 6728–6731.

[22] J. de Jesús Rubio, M. A. Hernandez, F. J. Rosas, E. Orozco, R. Balcazar, and J. Pacheco, "Genetic high-gain controller to improve the position perturbation attenuation and compact high-gain controller to improve the velocity perturbation attenuation in inverted pendulums," *Neural Netw*, vol. 170, p. 32–45, Feb. 2024.

[23] J. d. J. Rubio, "Bat algorithm based control to decrease the control energy consumption and modified bat algorithm based control to increase the trajectory tracking accuracy in robots," *Neural Netw*, vol. 161, p. 437–448, Apr. 2023.

[24] J. de Jesús Rubio et al., "References tracking and perturbations reconstruction in a cartesian robot," *Int. J. of Intel. Robot. and Appl.*, Feb. 2024.

[25] L. Arturo Soriano et al., "PD control compensation based on a cascade neural network applied to a robot manipulator," *Frontiers in Neurorobotics*, vol. 14, Dec. 2020.

[26] A. D. Kuo, "The six determinants of gait and the inverted pendulum analogy: A dynamic walking perspective," *Human Movement Science*, vol. 26, no. 4, pp. 617–656, Aug. 2007.

[27] M. Vigne, A. E. Khoury, F. D. Meglio, and N. Petit, "Improving low-level control of the exoskeleton Atalante in single support by compensating joint flexibility," in *Proc. 2020 IEEE-RSJ Int. Conf. on Intel. Robots and Syst. (IROS)*. IEEE, Oct. 2020.

[28] A. Vallinas, A. Keemink, C. Bayón, E. van Asseldonk, and H. van der Kooij, "Momentum-based balance control of a lower-limb exoskeleton during stance," in *Proc. 2023 Int. Conf. on Rehabil. Robot. (ICORR)*. IEEE, Sep. 2023.

[29] M. C. Yildirim et al., "Co-ex: A torque-controllable lower body exoskeleton for dependable human-robot co-existence," in *Proc. 2019 IEEE 16th Int. Conf. on Rehabil. Robot. (ICORR)*. IEEE, Jun. 2019, pp. 605–610.

[30] X. Guo, Z. Zhou, Y. Gao, J. Mai, and Q. Wang, "Serial–parallel mechanism and controller design of a robotic brace for dynamic trunk support," *IEEE/ASME Trans. Mechatronics*, vol. 27, no. 6, pp. 4518–4529, Dec. 2022.

[31] R. Featherstone, *Rigid Body Dynamics Algorithms*. Springer US, 2008.

[32] A. F. Soliman and B. Ugurlu, "Robust locomotion control of a self-balancing and underactuated bipedal exoskeleton: Task prioritization and feedback control," *IEEE Robot. Autom. Lett.*, vol. 6, no. 3, pp. 5626–5633, Jul. 2021.

[33] M. C. Yildirim et al., "Design and development of a durable series elastic actuator with an optimized spring topology," *Proc. Inst. of Mech. Eng., Part C: J. of Mech. Eng. Sci.*, vol. 235, no. 24, pp. 7848–7858, Jun. 2021.

[34] R. Bajpai and D. Joshi, "Foot2hip: A deep neural network model for predicting lower limb kinematics from foot measurements," *IEEE/ASME Trans. Mechatronics*, vol. 28, no. 4, pp. 2248–2258, Aug. 2023.

[35] A. F. Soliman, P. Sendur, and B. Ugurlu, "3-d dynamic walking trajectory generation for a bipedal exoskeleton with underactuated legs: A proof of concept," in *Proc. 2019 IEEE 16th Int. Conf. on Rehabil. Robot. (ICORR)*. IEEE, Jun. 2019, pp. 599–604.

[36] M. Mistry, J. Buchli, and S. Schaal, "Inverse dynamics control of floating base systems using orthogonal decomposition," in *Proc IEEE Int. Conf. on Robot. and Autom.*, 2010, pp. 2406–3412.

[37] B. Ugurlu, E. Sariyildiz, A. T. Kansizoglu, E. C. Ozcinar, and S. Coruk, "Benchmarking torque control strategies for a torsion-based series elastic actuator," *IEEE Robot. Autom. Mag*, vol. 29, no. 2, pp. 85–96, Jun. 2022.
[38] S. Oh and K. Kong, "High-precision robust force control of a series elastic actuator," *IEEE/ASME Trans. Mechatronics*, vol. 22, no. 1, pp. 71–80, Feb. 2017.
[39] R. Di Marco et al., "Experimental protocol to assess neuromuscular plasticity induced by an exoskeleton training session," *Methods and Protocols*, vol. 4, no. 3, p. 48, Jul. 2021.
[40] M. Vukobratovic and B. Borovac, "Zero-moment point - thirty five years of its life," *Int. J. of Humanoid Robot.*, vol. 01, no. 01, p. 157–173, Mar. 2004.
[41] G. Menga and M. Ghirardi, "Lower limb exoskeleton for rehabilitation with improved postural equilibrium," *Robotics*, vol. 7, no. 2, Jun. 2018.



Ahmed Fahmy Soliman (S'20) received his Ph.D. degree in Mechanical Engineering from Ozyegin University, Türkiye, in 2023. He currently holds a post-doctoral researcher position at the Biomechatronics Laboratory of Ozyegin University, Türkiye. His research interests are dynamic locomotion control of legged systems.



Sinan Coruk received his master's degree in Mechanical Science from Ozyegin University, Türkiye, in 2021. During his graduate studies, he focused on the design of series elastic actuators and torque-controllable exoskeletons. His main research interest is the development of exoskeletons with safe and dependable interaction capabilities.



Mehmet C. Yildirim (S'15) received his master's degree in Mechanical Engineering from Ozyegin University, Turkey, in 2018. He currently works as a Research Associate in Technical University of Munich and Munich Institute of Robotics and Machine Intelligence, Germany. His research focus includes compliant/tactile robot and actuators, elasticities on the robot structures.



Deniz Ugur received his bachelor's degree in Computer Science from Ozyegin University, Türkiye, in 2019. He is currently working toward his master's degree at the School of Computing Science of Simon Fraser University, Canada. His research interest is the development of fast and deterministic real-time operating systems for robots.



Suleyman Can Cevik received his bachelor's degree in Mechanical Engineering from Ozyegin University, Türkiye, in 2020. He is currently working toward his master's degree in Mechanical Engineering at the Robotics Laboratory of Ozyegin University, Türkiye. His research interest is safe and dependable human-robot interfaces for exoskeletons.



Burak Ozkaynak received his bachelor's degree in Mechatronics Engineering from Bahcesehir University, Türkiye, in 2020. He is currently working toward his master's degree in Mechanical Engineering at the Biomechatronics Laboratory of Ozyegin University, Türkiye. His research interest is motion planning and locomotion control of legged systems.



Polat Sendur received his Ph.D. degree in Mechanical Engineering from University of Michigan, USA, in 2002. He was a Simulation Expert with Tec-Masters Inc., USA, from 2002 to 2004. From 2004 to 2006, he worked with Robert Bosch Corporation, USA. From 2006 to 2016, he worked as Team Leader with Vehicle Dynamics and NVH, Ford Otosan, Türkiye. He currently holds an Assoc. Prof. position in Ozyegin University, Türkiye. He is working in the field of vibrations and acoustics.



Barkan Ugurlu (S'08-M'10-SM'23) received his Ph.D. degree in Electrical and Computer Engineering from Yokohama National University, Japan, in 2010. From 2010 to 2015, he worked as a researcher at the Istituto Italiano di Tecnologia, Italy, Toyota Technological Institute, Japan and Computational Neuroscience Laboratories of ATR, Japan. In 2015, he joined Ozyegin University, Türkiye and currently holds an Assoc. Prof. position. He is working in the field of locomotion control of legged systems.